MEASUREMENT OF $\sigma_{tot}(\bar{p}p)$ IN THE MOMENTUM RANGE BETWEEN 400 AND 700 MeV/c
— PHYSICS BACKGROUND AND TECHNICAL ASPECTS —

Kenzo NAKAMURA
Department of Physics, University of Tokyo. Tokyo

Measurement of $\sigma_{tot}(\bar{p}p)$ in the Momentum Range between 400 and 700 MeV/c
— Physics Background and Technical Aspects —

K. Nakamura
Department of Physics, University of Tokyo

(Talk presented at the 7th KEK Summer School, August, 1979)

1. Introduction

A group from University of Tokyo and Hiroshima University has just finished a low momentum $\bar{p}p$ experiment performed at the K3 beam channel of KEK. The primary purpose of this experiment is to investigate the famous S(1936) resonance, which is a candidate of a baryonium, an exotic meson composed of two quarks and two antiquarks. Although the observation of the S(1936) resonance has been reported in several experiments so far, its very existence has come into question quite recently.

In our experiment we have measured $\sigma_{tot}(\bar{p}p)$ with good precision and good mass resolution at beam momenta between 400 and 700 MeV/c. At the same time, we have measured $\sigma(\bar{p}p \to$ all neutral final states) and forward $d\sigma/d\Omega$ $(\bar{p}p \to \bar{p}p)$ in the same momentum range. Through these measurements, it is hoped to obtain firm evidence on the existence or non-existence of

the S(1936), and to determine its properties if it exists.

Although the analysis of the experiment is in progress, we do not yet have much results even in a preliminary form. Thus my talk will be mainly concentrated on physics background and technical aspects of the experiment. First, a short review will be presented on the baryonium and especially previous experimental results on the S(1936). Next, I will summarize basic knowledge on the total cross section and forward elastic scattering. Various methods to measure the total cross section will then be discussed. Finally, description of the experiment will be given, emphasizing its technical aspects.

2. Baryoniums

2. 1. Quark model and exotic states

Before discussing the baryonium, it is necessary to explain exotic states (or exotic resonances) which are not expected to exist in a standard quark model [1]. A "standard quark model" I mean is the one which has the following three basic ingredients:

(i) A quark bears a flavor which is connected to the observable quantum numbers. There are quark flavors of u, d, s and c, which are firmly established; b, which is believed to compose the Υ family together with its antiquark $\bar{b}$; t, which is under extensive search at high-energy e^+e^- colliding-beam facilities; and even more ?

(ii) A quark also bears a hidden degree of freedom, which makes an SU(3) colour space. The observable states must be colour-singlet, or colourless.

(iii) Mesons and baryons are composed of $q\bar{q}$ and qqq, respectively, where q stands for any quark and $\bar{q}$ for any antiquark.

Here we admit the first two statements and pay our attention to the last statement. This only reflects rather conservative view on hadron spectroscopy, i.e., the established mesons and baryons can be classified by only considering the $q\bar{q}$ and qqq quark configurations. In fact, multiquark states such as $(q\bar{q})^n$, $n \geq 2$ or $q^4\bar{q}$ can have an integral baryon number and can make a colour-singlet. To summarize, a stable (in a sense that the width $\Gamma \lesssim 100$ MeV) hadron is called exotic if its quark configuration is other than $q\bar{q}$ or qqq. The following are some examples of exotic hadrons.

(Example 1) A baryonium is an exotic meson whose quark configuration is $qq\bar{q}\bar{q}$. (A baryonium is frequently denoted as M_4 while an ordinary meson is denoted as M_2.)

(Example 2) If there exists Z_1^* or Z_0^* resonance in K^+p or K^+n system; it must have the $qqqq\bar{q}$ configuration, since for example, the proton and K^+ have the quark configurations of uud and $u\bar{s}$, and none of constituent quarks can annihilate with its antiquark.

(Example 3) There are some experimental evidence for dibaryon resonances [2], which may have a six quark configuration [3].

2.2. Theoretical requirement for the existence of the baryoniums and their expected properties

The existence of the baryoniums was first predicted by a duality argument [4]. Duality [5] as applied to the meson-meson and meson-baryon system has achieved much success. For baryon-antibaryon scattering, one can write a dual quark diagram shown in fig. 1, and it is clearly understood that ordinary-meson Regge poles are exchanged in the t-channel. If one applies duality to the baryon-antibaryon system, it requires the s-channel resonances whose quark configuration is $qq\bar{q}\bar{q}$. Therefore whether the required exotic $qq\bar{q}\bar{q}$ resonances (baryoniums) exist or not is a critical problem to duality.

Some of the important properties of baryoniums are as follows:

(i) A baryonium is inhibited to dacay into two ordinary mesons (figs. 2a and 2b). Its allowed decay modes are baryon-antibaryon pair (fig. 3a) or baryon-antibaryon plus one or more ordinary mesons (fig. 3b).

(ii) A baryonium has high mass, yet it has a narrow width near the baryon-antibaryon threshold.

(iii) A baryonium can have <u>exotic quantum numbers</u>. In particular, charge ± 2 states are possible.

Property (i) is required to suppress the appearence of a baryonium in the lowest order duality diagram of meson-meson scattering, since otherwise it would upset the successful duality constraints in meson-meson scattering. To inhibit dual quark diagrams shown in fig. 2, the usual OZI rule must be extended to the following form [Freund-Waltz-Rosner rule [6]]:

(A) At the vertex of three hadrons, at least one quark (or antiquark) line should be exchanged between any pair of hadrons. (This inhibits the diagram shown in fig. 2a.)

(B) A quark line and an antiquark line originating from the

same hadron should not annihilate. (This inhibits the diagram shown in fig. 2b.)

Property (ii) is a direct consequence of property (i). Property (iii) is an interesting consequence of the $qq\bar{q}\bar{q}$ configuration. Exotic quantum numbers are the quantum numbers which ordinary mesons cannot take. Denoting the total spin, total orbital angular momentum and total angular momentum of the $q\bar{q}$ system as $\vec{S}$, $\vec{L}$ and $\vec{J}$, the quantum numbers of ordinary mesons are constrained as $\vec{J} = \vec{L} + \vec{S}$, $P = (-1)^{L+1}$ and $C = (-1)^{L+S}$. Thus ordinary mesons cannot take exotic quantum numbers, $J^{PC} = 0^{--}$, 1^{-+} etc., which however baryoniums can take. Charge ± 2 is also clearly impossible for $q\bar{q}$ states.

2. 3. Experimental search for baryoniums

A good deal of experimental effort has been made in search of baryoniums [7]. The key signals of the baryonium are the properties just mentioned. Experiments are mostly classified into two categories; one is resonance search in the $\bar{p}p$ direct channel and the other is bump hunting in production experiments in effective mass distributions of $\bar{B}B$, $\bar{B}B\pi$ etc., or charge ± 2 meson states. Listed below are some baryonium candidates which have been reported. All narrow resonances, however, have yet to be confirmed to be there. On the other hand, wide enhancements seen in the direct $\bar{p}p$ channel seem established, but at present it is not clear whether they are really baryoniums.

Baryonium candidates reported in the $\bar{p}p$ interactions

(i) The S(1936) resonance. This will be discussed in detail in the next subsection.

(ii) Wide enhancements observed in $\sigma_{tot}(\bar{p}p)$, $\sigma(\bar{p}p \to \bar{p}p)$, $\sigma(\bar{p}p \to \bar{n}n)$, and various annihilation cross sections [7]. They are called T (mass $\sim$ 2190 MeV, $\Gamma \sim$ 150 MeV) and U (mass $\sim$2350 MeV, $\Gamma \sim$ 200 MeV). In addition, some evidence is reported on V (mass $\sim$ 2480 MeV, $\Gamma \sim$ 250 MeV).

(iii) Pavlopoulos et al. [8] observed a few narrow enhancements in the energy spectrum of γ-rays in a stopped $\bar{p}$ experiment. Possibly they are signals of baryonium states below $\bar{p}p$ threshold.

Baryonium candidates reported in production experiments

(i) Benkheiri et al. [9] observed two narrow enhancements (2020 MeV with $\Gamma \sim$ 24 MeV and 2200 MeV with $\Gamma \sim$16 MeV) in the $\bar{p}p$ effective mass distribution in the reaction $\pi^- p \to \pi^- p_{forward}$ $(\bar{p}p)$ (see fig. 4). The experiment was performed at CERN using the Ω spectrometer. However, these enhancements are not seen in the reaction $\pi^+ p \to \pi^+ p_{forward}$ $(\bar{p}p)$, recently performed at BNL using the Multi-Particle Spectrometer [10].

(ii) Armstrong et al. [11] observed a narrow enhancement (2460 MeV, $\Gamma \sim$ 15 MeV) in the $\bar{\Lambda}p\pi^+$ mass spectra in the reaction $K^+ p \to \bar{\Lambda}_{forward}\, p\pi^+ n$, performed at CERN using, again, the Ω spectrometer. It should be noted that $\bar{\Lambda}p\pi^+$ system has an exotic quantum number (charge +2).

2. 4. The S(1936) resonance

At the time of the Tokyo conference, the S resonance seemed

to be firmly established. Four different experiments [12-15] reported its observation in σ_{tot} [12,13,15], $\sigma(\bar{p}p \to \bar{p}p)$ [13,14] and charged-prong annihilation cross sections [13,14]. These experiments are summarized in table 1 and their main results are shown in figs. 5 - 8. It should be also noted that in an Ω spectrometer experiment [9] a narrow enhancement was observed at the $\bar{p}p$ effective mass corresponding to the S resonance, although it was statistically less significant than the 2020 and 2200 MeV enhancements.

The observed properties of the S resonance are:

(i) mass $\sim$ 1936 MeV, very near the $\bar{p}p$ threshold;

(ii) very narrow width, $\Gamma \lesssim 4$ MeV;

(iii) large elasticity, $\sigma(\bar{p}p \to \bar{p}p)/\sigma_{tot} \approx 0.7$;

(iv) peak observed in the elastic channel, but not in the charge-exchange channel.

From the first three properties, the S resonance has been considered almost certainly to be a baryonium. The last observation would be puzzling if the S resonance should have a definite isospin, 0 or 1. This can be seen as follows. Denoting the isospin 0 and 1 amplitudes as A_0 and A_1, the elastic and charge-exchange amplitudes are written as

$$A(pp \to pp) = \tfrac{1}{2}(A_1 + A_0)$$

$$A(pp \to nn) = \tfrac{1}{2}(A_1 - A_0).$$

To explain the observed fact, one needs both isospin 0 and 1 amplitudes; they destructively interfere in the charge-exchange

channel. Both amplitudes might be resonant, or either might be resonant and the other non-resonant background. Certainly it seemed an urgent problem to determine the quantum number, especially the isospin of the S resonance.

To our surprise, however, an LBL group, which has performed a series of $\bar{p}p$ experiment at BNL, has recently reported [16,17] that no S-resonance enhancement has been observed in all of their measurements

(i) $\sigma(\bar{p}p \to \bar{n}n)$

(ii) backward elastic scattering cross section

(iii) $\sigma_{tot}(\bar{p}p)$.

Non-observation of the S resonance in the charge-exchange reaction is consistent with the previous results. Also, considering the peculiarity of the backward direction and interfering I = 0 and I = 1 amplitudes, some sophisticated theory might succeed in explaing the disappearance of the S-resonance enhancement in the backward elastic scattering. However, the total cross section result of the LBL group shown in fig. 9 is definitely in disagreement with the previous results.

After all, the very existence of the S resonance has become a burning question, together with the disappearance of the 2020 and 2200 MeV enhancements in the MPS production experiment [10] (see subsect. 2.3). New measurements with fine mass resolution and good accuracy (both statistical and systematic) are highly needed to settle the problem. Our experiment is clearly the one required, and we hope we can shortly give an answer to this question.

2. 5. Note added: some models for the baryonium

Before closing this section, I would like to briefly mention some models for the baryonium.

There are mainly two alternative views on the nature of the baryonium. In one view, which is prevailing, a baryonium is composed of two quarks and two antiquarks, as already discussed. In the other view, however, a baryonium is a baryon-antibaryon system held together by nuclear forces [18]. The latter view, which is mainly developed by nuclear physicists, might be appropriate for subthreshold baryoniums.

In a string-junction model of Rossi and Veneziano [19], and Imachi, Otsuki and Toyoda [20], a conserved pair of junction and antijunction is introduced in addition to the quarks and antiquarks. There appear three types of baryoniums; $M_4^2(qq\bar{q}\bar{q};J\bar{J})$, $M_2^2(q\bar{q};J\bar{J})$ and $S_0^2(J\bar{J})$. In this type of model, the selection rules of Freund-Waltz-Rosner [6] are extended to include junctions, and topological structure of diagrams is closely connected with decay rates of baryoniums.

Of particular interest is a colour molecule model of Chan Hong-Mo and Högaasen [21], in which a baryonium is realized as a diquark (qq)-antidiquark ($\bar{q}\bar{q}$) system (which is called "diquonium") bound by colour confining forces. A diquark is a coloured object (colour non-singlet), and hence the name of "colour molecule". In order that such a system be metastable, the diquark is separated from the antidiquark by an orbital angular momentum $L > 0$, and this condition naturally suppresses the baryonium decay into two ordianry mesons without resorting

to new, ad hoc, and therefore unsatisfactory (as Hong-Mo says) selection rules. Exploiting the knowledge obtained for ordinary hadron dynamics, this model has a great predictive power for the rich spectrum of the baryonium. In this regard, however, the model is being challenged by the recent experimental indications that the narrow baryonium candidates reported so far do not really exist.

3. Total cross sections and forward elastic scattering

3. 1. General

Let me now turn to a quite different subject, total cross sections and forward elastic scattering [22].

We write the differential cross section for the elastic scattering in the c.m. system as

$$\left(\frac{d\sigma}{d\Omega^*}\right)_{el} = \left|f(E^*, \theta^*)\right|^2 , \tag{1}$$

which defines the scattering amplitude $f(E^*, \theta^*)$. We also define, for later convenience, another amplitude $F(t)$ by

$$\left(\frac{d\sigma}{dt}\right)_{el} = \frac{\pi}{p^{*2}} \left(\frac{d\sigma}{d\Omega^*}\right)_{el} \equiv \left|F(t)\right|^2 . \tag{2}$$

The optical theorem relates the imaginary part of the forward scattering amplitude to the total cross section:

$$\mathrm{Im}\ f(\theta^*=0) = \frac{p^*}{4\pi}\,\sigma_{tot} \tag{3}$$

$$\mathrm{Im}\ F(0) = \frac{1}{4\sqrt{\pi}}\,\sigma_{tot} . \tag{4}$$

From eqs. (1) - (4), we obtain

$$\left(\frac{d\sigma}{d\Omega^*}\right)_{\theta^*=0} = \left(\frac{p^* \sigma_{tot}}{4\pi}\right)^2 (1+\rho^2) \qquad (5)$$

$$\left(\frac{d\sigma}{dt}\right)_{t=0} = \frac{\sigma^2_{tot}}{16\pi} (1+\rho^2) \ , \qquad (6)$$

where ρ is the real-to-imaginary ratio of the forward scattering amplitude

$$\rho = \frac{\text{Re } f(\theta^*=0)}{\text{Im } f(\theta^*=0)} = \frac{\text{Re } F(0)}{\text{Im } F(0)} \ . \qquad (7)$$

Let us now consider the angular distribution of the elastic scattering. It is customary to divide the angular interval into the following five regions according to the values of t [22]:

(i) Coulomb region $[t \lesssim 0.001 \ (\text{GeV/c})^2]$

(ii) Coulomb-nuclear interference region $[0.001 \lesssim t \lesssim 0.01]$

(iii) Diffraction region $[0.01 \lesssim t \lesssim 0.5]$

(iv) Large angle region $[t \gtrsim 0.5]$

(v) Backward region $[u \sim 0]$.

Region (i) is well understood and not very interesting. Region (ii) is most interesting for the present experiment and is further discussed below. The diffraction region is characterized by a smooth exponentially falling differential cross section: in a limited t interval, it can be parametrized as

$$\frac{d\sigma}{dt} = a \exp(-bt) \ . \qquad (8)$$

Regions (iv) and (v) are not relevant to the present experiment, and are not discussed here.

When the Coulomb amplitude $F_C(t)$ is non-negligible compared to the nuclear amplitude $F_N(t)$, the full amplitude is given by

a coherent sum of both amplitudes, and we write the differential cross section as

$$\frac{d\sigma}{dt} = \left| F_N(t) + F_C(t) \right|^2 = \left|F_N\right|^2 + 2\text{Re}(F_N^* F_C) + \left|F_C\right|^2$$

$$\equiv \frac{d\sigma_N}{dt} + \frac{d\sigma_{NC}}{dt} + \frac{d\sigma_C}{dt} \ . \qquad (9)$$

The Coulomb amplitude for $\bar{p}p$ or pp scattering is known to be

$$F_C^{\bar{p}p}(t) = -F_C^{pp}(t) = \frac{2\sqrt{\pi}\hbar c\alpha}{\beta t} \mathcal{F}(t) \ e^{-i\delta(t)} \ , \qquad (10)$$

where α is the fine structure constant, β is the lab. velocity of the incident particle, $\delta(t)$ is the Coulomb phase which is calculated with slight model dependence, and $\mathcal{F}(t)$ is the Coulomb form factor given by

$$\mathcal{F}(t) = G^2(t) = (1 + t/0.71)^{-4} \ , \qquad (11)$$

where G(t) is the electromagnetic form factor of the proton. For small t, the elastic differential cross section due to the nuclear interaction is assumed to be extrapolated from the diffraction region:

$$\frac{d\sigma_N}{dt} = \left(\frac{d\sigma_N}{dt}\right)_{t=0} \exp(-bt) \ . \qquad (12)$$

Then the nuclear amplitude is written as

$$F_N(t) = \text{Im } F_N(0) \ (\rho+i) \exp(-\tfrac{1}{2}bt)$$

$$= \frac{\sigma_{tot}}{4\sqrt{\pi}\hbar c} \ (\rho+i) \exp(-\tfrac{1}{2}bt) \ , \qquad (13)$$

where ρ is assumed to be constant for small t ($t \lesssim 0.01$). Putting eqs. (10) and (13) into eq. (9), the $\bar{p}p$ forward differential

cross section is written in terms of σ_{tot}, ρ and b as

$$\frac{d\sigma}{dt} = 4\pi\left(\frac{\alpha\hbar c}{\beta t}\right)^2 \mathcal{F}^2(t) + \left(\frac{\sigma_{tot}}{4\sqrt{\pi}\hbar c}\right)^2 (1+\rho^2)\exp(-bt)$$

$$+ \frac{\alpha\sigma_{tot}}{\beta t}\mathcal{F}(t)\exp\left(-\frac{1}{2}bt\right)(\rho\cos\delta - \sin\delta) \quad . \quad (14)$$

As an example, fig. 10 shows the forward $\bar{p}p$ defferential cross section at 1.2 GeV/c [23], where the distribution is fitted using eq. (14) and components of $d\sigma/dt$, i.e., Coulomb part, nuclear part and interference part are separately indicated.

3. 2. How to measure the total cross section

There are basically three methods to measure the total cross section. One is to directly count the number of interactions. This method is mostly used in bubble chamber experiments or pp total cross section measurements at the CERN ISR. In either case, the elastic scattering in extreme forward directions cannot be measured and so must be corrected. The second method to measure the total cross section is known as the transmission method, where one counts particles transmitted a target without interacting in it. Since we adopted this method in the present experiment, a further discussion is given below. The last method is an indirect method where one deduces σ_{tot} from the forward elastic differential cross section, using the optical theorem. This method has been applied at the CERN ISR and gas-jet target experiments at Fermilab and IHEP. It should be stressed that in all three methods, we need to know the parameters ρ and b in order to make corrections

or to apply the optical theorem. These parameters must be taken from other experiments, or determined in the same experiment, or guessed from theoretical considerations.

I now explain the transmission experiment in some detail. The standard equipment (see fig. 11) consists of a system of counters to count the incoming particles and a series of concentric transmission counters, each subtending a different solid angle Ω_i with respect to the target. We can define the partial cross section σ_i measured by the i-th transmission counter:

$$\sigma_i = \int_{\Omega_i}^{4\pi}\left\{\frac{d\sigma_C}{d\Omega} + \frac{d\sigma_{NC}}{d\Omega} + \frac{d\sigma_N}{d\Omega}\right\} d\Omega + \sigma_{inel} \quad . \quad (15)$$

The total cross section is written as

$$\sigma_{tot} = \int_{\Omega_i}^{4\pi}\left(\frac{d\sigma_N}{d\Omega}\right) d\Omega + \int_0^{\Omega_i}\left(\frac{d\sigma_N}{d\Omega}\right) d\Omega + \sigma_{inel} \quad . \quad (16)$$

From eqs. (15) and (16) we have

$$\sigma_i = \sigma_{tot} + \int_{\Omega_i}^{4\pi}\left\{\frac{d\sigma_C}{d\Omega} + \frac{d\sigma_{NC}}{d\Omega}\right\} d\Omega - \int_0^{\Omega_i}\left(\frac{d\sigma_N}{d\Omega}\right) d\Omega \quad , \quad (17)$$

and σ_{tot} is obtained by the extrapolation to zero solid angle. In a so called <u>good geometry transmission experiment</u>, each transmission counter subtends the solid angle well within the diffraction peak, and the smallest counter covers the Coulomb region completely. Then the $d\sigma_C/d\Omega$ term in eq. (17) is negligible and $d\sigma_N/d\Omega$ term can be extrapolated to zero solid angle. However the $d\sigma_{NC}/d\Omega$ term must be corrected before the extrapolation is performed (see fig. 12), and for this purpose the parameters ρ and b must be known. In eq. (15), particle

emission into the solid angle Ω_i from the inelastic reactions is neglected. However, it can also be extrapolated to zero solid angle on an equal footing with $d\sigma_N/d\Omega$ in eq. (17).

In practice, the incoming beam is absorbed not only by the target, but also by other materials before and behind the target. To take account for this effect, we usually prepare two identical target cells: one is full of target material and the other is empty. Let N_{0F} and N_{0E} be the number of incident particles and N^i_{1F} and N^i_{1E} the number of particles counted by the i-th counter, where the subscripts F and E represent full target and empty target, respectively. For the case of full target we have the relation

$$N^i_{1F} = N_{0F}\, \eta_1 \eta_2 \exp(-\sigma_i n) , \qquad (18)$$

where η_1 and η_2 account for the absorption before and behind the target and n is the number of target particles per cm^2. For the case of empty target,

$$N^i_{1E} = N_{0E}\, \eta_1 \eta_2 . \qquad (19)$$

From eqs. (18) and (19), we thus obtain the expression for σ_i in terms of measurements with both targets:

$$\sigma_i = \frac{1}{n} \left\{ \ln \frac{N_{0F}}{N^i_{1F}} - \ln \frac{N_{0E}}{N^i_{1E}} \right\} . \qquad (20)$$

4. Description of the experiment

4. 1. General

The main purpose of the present experiment is to investi-

gate possible narrow structures (in particular the S resonance) in the $\bar{p}p$ total cross section in the momentum range between 400 and 700 MeV/c. It is also aimed to measure the cross section of the all neutral final states and forward elastic differential cross section at the same time.

The requirements to be met to investigate narrow structures are good mass resolution, high statistical accuracy and small systematic errors. In the present experiment, the mass resolution for the $\bar{p}p$ system of within ± 2 MeV has been achieved and the $\bar{p}p$ total cross section has been measured with statistical accuracy of ± 1.5 % in the S region and ± 2 % otherwise, and with a total systematic error of order 1 %.

A unique feature which distinguishes the present experiment from other total cross section measurements is the use of multiwire proportional chambers and a magnetic spectrometer instead of conventional transmission counters. This fact has been essential to achieve small and well controlled systematic errors. The most important features are:

(i) The momentum and trajectory of the incoming and transmitted antiprotons have been measured event by event. Specifically this means that we can always use the same beam phase space by making appropriate cuts on the incoming trajectory.

(ii) Particle identification has been done with a good accuracy (fractional π^- contamination $\sim$ 1/5000).

(iii) The beam momentum has always been calibrated using precisely measured magnetic field of the spectrometer magnet to an absolute accuracy of ± 0.5 % and relative (point-to-point)

accuracy of ±0.05 %.

It should be noted that some total cross section measurements were made with better statistical accuracy than ours, but the systematic errors originating from usually not well-known beam quality could be rather large and difficult to estimate.

During data-taking runs, we have also taken care of the following points so as not to produce spurious narrow structures, or not to miss real narrow structures:

(i) Avoid the momentum-dependent systematic errors.

(ii) Avoid time-dependent variation of the systematic errors.

(iii) Each measurement at a certain beam momentum has a 50 % overlap in the beam momentum acceptance with the measurements at the neighbouring beam momenta.

4. 2. Apparatus

A plan view of the apparatus including the beam transport system is shown in fig. 13.

Beam channel

The experiment has been performed at the K3 beam line of the KEK proton synchrotron. A partially separated antiproton beam has been produced from a Pt target (40 mm long and 10 mm in diameter or 6 X 10 mm^2 in cross section) in a slow extracted proton beam. The K3 beam line has the two operation modes: one is the long-focus mode (K3-L) with high momentum resolution at the sacrifice of a beam intensity, and the other is the short-focus mode (K3-S) with the maximum beam intensity at the sacrifice of the resolution. We have taken advantage of the

high resolution of the K3-L mode. The parameters of the K3-L mode are listed in table 2 and the beam optics is shown in fig. 14.

The momentum bite of the antiproton beam has been limited to ±2 % by the momentum slit at the momentum-dispersive focus. The beam momentum has been measured by a hodoscope placed also at the momentum-dispersive focus. The momentum resolution is calculated to be ±0.3% at 500 MeV/c, taking into the Coulomb multiple scattering by thin metal windows of a vacuum duct, scintillation counters, proportional chambers, and etc. Fig. 15 shows a flux of the antiproton beam per 10^{12} extracted 12 GeV protons on the Pt target 40 mm long and 6 X 10 mm^2 in cross section. It should be noted that the focusing of the extracted proton beam on the K3 target was not satisfactory, resulting rather low targetting efficiency. This is the reason why we used a production target of wide cross section at the sacrifice of the $\pi/\bar{p}$ separation. (At 500 MeV/c and 800 MeV/c $\pi/\bar{p} \sim 300$ and 100, respectively.) If the focusing of the primary proton beam is improved, the flux of the antiproton beam would increase at least by a factor of 1.5.

Liquid hydrogen target

Two identical target cells, one filled with liquid hydrogen and the other empty, were placed in the same vacuum chamber. To change full and empty targets, the vacuum chamber could be moved in a few minutes by a step motor along a rail fixed to a support structure. The reproducibility of the target positions

was excellent (of order 10 μm). The target cell had a double cylinder structure: the inner cylinder 65 mm in diameter was made of thin Al and the outer one 74 mm in diameter was made of stainless steel. The outer cylinder had flanges at both ends to which mylar sheets were glued and tightly held by cover flanges. The length of liquid hydrogen along the beam axis was 85 mm. The temperature of the liquid hydrogen has been controlled to within 0.1°K.

The above described liquid hydrogen target system was designed to meet the requirement on the mass resolution for the $\bar{p}p$ system and to minimize various systematic errors in the total cross section measurement. Some important points are:

(i) With 85 mm long liquid hydrogen target, the mass resolution for the $\bar{p}p$ system is about $\pm$2 MeV at 500 MeV/c and $\pm$1.5 MeV at 700 MeV/c.

(ii) The density of the liquid hydrogen ρ_H depends on the temperature T. At around 21°K the relation $\Delta\rho_H/\rho_H \sim 0.02\Delta T$ holds. Since the temperature has been controlled to within 0.1°K, the error of σ_{tot} resulting from the uncertainty of ρ_H is only about 0.2 %.

(iii) Bubbles in the liquid hydrogen effectively reduces ρ_H. With the target cell of the double cylinder structure, it was possible to suppress bubbles inside the inner cylinder, since bubbles were mostly produced by absorbing heat radiation from outside.

(iv) Since the pressure difference between inside and outside of the target cell is about 1 kg/cm^2, the shape of the mylar

window is convex and the length of the liquid hydrogen traversed is dependent on the trajectory of the beam particles. The flange structure of the target cell allows a rather small curvature of the mylar windows.

Counters and multiwire proportional chambers

The scintillation counters C1, C2 and C3 defined the incoming antiprotons and C4 and C6 detected transmitted antiprotons. The 3 mm thick counters C3 and C4 placed just before and behind the liquid hydrogen target had circular shapes of 40 mm and 70 mm in diameter, respectively. The counter C6 was placed behind the spectrometer magnet and its dimension was 660 X 440 X 5 mm^3. The counters C1 ~ C4 were viewed by two RCA 8575 photomultipliers, while C6 was viewed by four. Pulse height and time of flight information from each counter was recorded. For pulse height measurement, photomultiplier outputs were added and fed to an ADC channel. For time of flight measurement, the counter C1 provided common start signal to a TDC module, and signals from C2 ~ C6 stopped each TDC channel. Mean timer modules were used for wide counters C2 and C6 to improve time resolution. For C6, time differences between up and down, and between right and left photomultiplier signals were recorded, giving a rough two-dimensional coordinate where the particle traversed it.

In order to detect charged particles coming from the target, a cylindrically shaped scintillation counter surrounding the target was placed inside the vacuum chamber and was optically

coupled to a photomultiplier outside the chamber. Before and behind the target vacuum chamber there were also scintillator walls having 45 mm and 75 mm diameter holes through which incoming and transmitted antiprotons passed. These counters covered about 95 % solid angle around the target and served to measure $\sigma(\bar{p}p \to \text{all neutrals})$. An exploded view around the target region is shown in fig. 16.

The beam momentum was measured by a 36 channel hodoscope placed at the momentum-dispersive focus of the K3 beam line, and the momentum of the transmitted particle was measured by a hodoscope placed at another momentum-dispersive focus behind C6, which consisted of 26 overlapping scintillation counters making 51 channels. Additionally, a 5 X 5 thin hodoscope was placed between the quadrupole magnets Q9 and Q10 to aid the track reconstruction using multiwire proportional chambers (MWPC).

The trajectories of the incoming and transmitted antiprotons were measured by five MWPC's of two-dimensional readout. Cathode readout was done by means of delay lines, and position resolution of ± 1 mm was obtained. Fig. 17 shows schematic representation of the MWPC readout. Each cathode wire was connected to a tap of the delay line (2 mm cathode wire spacing, and 20 nsec delay per tap for the small chambers $1 \sim 4$ and 10 nsec delay per tap for the large chamber 5). Induced charges on the cathode wires propagated to both ends of the delay line and were amplified and discriminated by constant-fraction discriminators. The discriminator outputs were fed to a TDC module and the time difference of the signals from both ends of the delay line gave

the center of gravity of the induced charges. To improve inherent limitation on counting rates of the delay line readout, a double TDC stop circuits were introduced so that we could still obtain position information even though another stop signal came while the TDC gate was open.

Magnetic spectrometer

The magnetic spectrometer consisted of a quadrupole doublet and a bending magnet (max. field 20 kG). Its angular acceptance was $x' = \pm 120$ mr, $y' = \pm 40$ mr and $\Delta\Omega = 15$ msr, and the maximum transmissible momentum bite was $\Delta p/p = \pm 15$ %. The magnetic fields of the bending magnet were measured as precisely as possible, and provided a powerful means to calibrate the beam momentum. The beam momentum could be known to the absolute accuracy of ± 0.5 % and the relative (point-to-point) accuracy of ± 0.05 %.

4. 3. Experimental procedure and very preliminary results

The data-taking has been carried out from May to July 1979, over six KEK accelerator operation periods (one period is two weeks long). The measurements have been performed with a 2 % step in the beam momentum from 410 to 720 MeV/c. Since the momentum bite of the beam has been ± 2 %, we have never missed possible structures in the total cross section as narrow as the mass resolution of the present experiment. To avoid systematic errors due to possible long-term variation of the detector system, each momentum interval was measured several times in different accelerator periods. The alternation of the full and empty tar-

gets was done within one hour. A total of about 1.5×10^7 events were recorded, of which about 60 % were taken with target full and the rest with target empty. About 50 % of events will be retained for the final analysis after various cuts to guarantee clean incoming antiprotons of known momentum and trajectory.

An event was triggered by a time coincidence C1·C2·C3 and all relevant information was written on magnetic tapes. Although the timing of the trigger counters was adjusted to the antiproton, high counting rate of C1 caused considerable amount of accidental triggers due to pions when the discriminator threshold for C1 was set low enough to register all minimum ionizing particles. To suppress these accidental triggers, the discriminator threshold for C1 was set high to reject almost all minimum ionizing particles. In this way, more than 90 % triggers were due to antiprotons.

In the offline analysis, the identification of the antiproton was performed using pulse height and time of flight (TOF) information from trigger counters to a level of fractional pion contamination of 1/5000. Since the flight path length from C1 to C6 was about 16 m, those antiprotons and pions reached C6 were very cleanly separated. Using these events we could precisely determine the pulse height and TOF distributions from C1 ~ C4 for antiprotons and pions. In this sense, the linear electronics channels of the present experiment were self-calibrating and required no special calibration runs.

As a very preliminary analysis of the $\bar{p}p$ total cross section we have counted the number of antiprotons reached the counter

C6. The quantity $\ln N_B/N_T$ is plotted in fig. 18 for both full and empty targets, where N_B is the number of incoming antiprotons and N_T the number of transmitted antiprotons which reached C6. From this, the total cross section is calculated and plotted in fig. 19. The events used are about 60 % of those usable for the final analysis. The error bars are statistical only and no corrections are made for the effects of the Coulomb-nuclear interference and contamination of forward elastic scattering events. However, it is estimated that the net correction is not large (less than ± 2 %). Although this result is very preliminary, we see that there are no narrow structures in the entire momentum range with more than one-standard-deviation effect.

5. Conclusion

As we have seen in section 2, the baryoniums with the exotic quark configuration $qq\bar{q}\bar{q}$ have been extensively investigated both theoretically and experimentally. Until quite recently, it has generally been believed that there exist some narrow $\bar{p}p$ resonances which have expected properties of the baryonium. Thus, the recent experimental indication against the existence of the S resonance [16,17] has brought much surprise. Our preliminary result on the $\bar{p}p$ total cross section is also consistent with the nonexistence of the S resonance. These experimental results are clearly requiring reexamination of the baryonium physics.

References

1) See, for example, Quarks and Hadronic Structure, edited by G. Morpurgo (Plenum, N. Y., 1977);
J. J. J. Kokkedee, The Quark Model (Benjamin, N. Y., 1969).
2) T. Kamae et al., Phys. Rev. Lett. 38 (1977) 468;
H. Ikeda et al., Phys. Rev. Lett. 42 (1979) 1321;
I. A. Auer et al., Phys. Lett. 70B (1977) 475.
3) P. J. G. Mulders et al., Phys. Rev. Lett. 40 (1978) 1543;
C. W. Wong and K. F. Liu, Phys. Rev. Lett. 41 (1978) 82.
4) J. L. Rosner, Phys. Rev. Lett. 21 (1968) 950.
5) M. Fukugita and K. Igi, Phys. Reports 31 (1977) 237.
6) P. G. Freund, R. Waltz and J. Rosner, Nucl. Phys. B13 (1969) 237.
7) L. Montanet, Proc. 5th Int. Conf. on Experimental Meson Spectroscopy, Boston, 1977, edited by E. von Goeler and R. Weinstein (Northeastern Univ. Press, Boston, 1977) p. 260;
H. Yoshida, Proc. of the Meeting on Exotic States in Anti-proton-Nucleon Interactions, KEK, 1978 (Report KEK-79-1, in Japanese) p. 3.
8) P. Pavlopoulos et al., Phys. Lett. 72B (1978) 415.
9) P. Benkheiri et al., Phys. Lett. 68B (1977) 483.
10) Private communication from S. Ozaki; also see his lecture note in this volume.
11) T. A. Armstrong et al., Phys. Lett. 77B (1978).
12) A. S. Carroll et al., Phys. Rev. Lett. 32 (1974) 247.
13) V. Chaloupka et al., Phys. Lett. 61B (1976) 487.
14) W. Bruckner et al., Phys. Lett. 67B (1977) 222.

15) S. Sakamoto et al., Nucl. Phys. B, to be published.
16) M. Alston-Garnjost et al., Phys. Rev. Lett., to be published.
17) R. Tripp, Talk presented at the 1979 EPS Int. Conf. on High Energy Physics, Geneva, 1979.
18) T. E. O. Ericson, Proc. of 3rd European Symp. on Antinucleon-Nucleon Interactions, Stockholm, 1976, edited by G. Ekspong and S. Nilsson (Pergamon, Oxford, 1977) p. 3, and references therein.
19) G. C. Rossi and G. Veneziano, Nucl. Phys. B123 (1977) 507.
20) M. Imachi, S. Otsuki and F. Toyoda, Prog. Theor. Phys. 56 (1976) 551 and 57 (1977) 517;
M. Imachi and S. Otsuki, Prog. Theor. Phys. 59 (1978) 1290.
21) C. Hong-Mo and H. Hägaasen, Nucl. Phys. B136 (1978) 401.
22) An extensive review is given by G. Giacomelli, Phys. Reports 23C (1976) 123.
23) P. Jenni et al., Nucl. Phys. B94 (1975) 1.

Table 1. Summary of the experiments reported the observation of the S resonance.

	Carrol et at. BNL Ref. 12)	Chaloupka et al. CERN etc. Ref. 13)	Brückner et al. CERN-Heidelberg Ref. 14)	Sakamoto et al. Tokyo Ref. 15)
Method	Transmission counter	Bubble chamber	Counter	Bubble chamber
Measured	σ_{tot} ($\bar{p}p$) σ_{tot} ($\bar{p}d$)	σ_{tot} ($\bar{p}p$) $\sigma(\bar{p}p \to \bar{p}p)$ σ_{inel} (0,2,4,6 prongs)	$\sigma(\bar{p}p \to \bar{p}p)$ $\sigma(\bar{p}p \to$ charged mesons) $\sigma(\bar{p}p \to$ all neutrals)	σ_{tot} ($\bar{p}p$)
S resonance parameters				
Mass (MeV)	1932 ± 2	1935.9 ± 1.0	1939 ± 3	1935.5 ± 1.0
Γ (MeV)	9^{+4}_{-3}	$8.8^{+4.3}_{-3.2}$	$\lesssim 4$	2.8 ± 1.4
σ_{tot} (mb)	18^{+6}_{-3}	10.6 ± 2.4	—	14.5 ± 3.9
Other information	Possibly I = 1, but I = 0 not ruled out.	$\sigma(pp \to pp) = 7.0 \pm 1.4$ mb		

Table 2. K3 beam parameters (L-mode)

Momentum range	< 1.0 GeV
Production angle	0^o
Solid angle acceptance	4 msr
Horizontal	±120 mr
Vertical	±10.5 mr
Maximum transmissible Momentum bite	±2.7 %
Momentum resolution	±0.15 %
Electrostatic separator	
Electrode length	1.9 m
Gap	15 cm
Max. field (E_{max})	50 kV/cm
At the momentum slit	
Horizontal magnification	-4.39
Momentum dispersion	3.40 cm/(1 % δp/p)
Chromatic aberration	7.23 mm/(1 % δp/p)
At the mass slit	
Vertical magnification	-0.423
Vertical chromatic aberration	3.04 mm/(1 % δp/p)
Image separation between π and $\bar{p}$ at 500 MeV/c	58.3 mm at E_{max}
At the experimental focus	
Horizontal magnification	3.12
Vertical magnification	1.35
Momentum dispersion	0.0
Horizontal divergence	69.3 mr } (2σ)
Vertical divergence	24.5 mr } (2σ)

Figure captions

Fig. 1. Dual quark diagram for the baryon-antibaryon scattering.

Fig. 2. Inhibited diagrams for the baryonium decaying into the two ordinary mesons.

Fig. 3. Allowed diagrams for the baryonium decay.

Fig. 4. $\bar{p}p$ invariant mass distribution in the reaction $\pi^- p \rightarrow \pi^- p_{forward}$ ($\bar{p}p$) at 9 and 12 GeV/c, taken from ref. 9).

Fig. 5. $\bar{p}p$ and $\bar{p}d$ total cross sections measured by Carrol et al. [ref. 12)].

Fig. 6. $\bar{p}p$ total, inelastic (0+2+4+6 prongs), elastic and 0,2,4,6 prong cross sections measured by Chaloupka et al. [ref. 13)].

Fig. 7. $\bar{p}p$ inelastic (two or more prongs), elastic and neutral cross sections measured by Bruckner et al. [ref. 14)].

Fig. 8. $\bar{p}p$ total cross section measured by Sakamoto et al. [ref. 15)].

Fig. 9. $\bar{p}p$ total cross section multiplied by the beam momentum, measured by the LBL group [ref. 17)]. The data are preliminary and uncorrected. The dashed curve represents the results of Carrol et al. [12)]

Fig. 10. Forward elastic $\bar{p}p$ differential cross section at 1.2 GeV/c measured by Jenni et al. [ref. 23)]. (a) shows the details of the region of t where the Coulomb-nuclear interference is important. The individual contributions due to the nuclear scattering (curve b), the Coulomb scattering (curve c) and their interference (curve d) are shown. (b) displays the complete t-region used

for the fit.

Fig. 11. Typical experimental setup for a transmission counter experiment.

Fig. 12. Schematic representation of the dependence of $\sigma_i(\Omega)$ on the solid angle Ω_i.

Fig. 13. Plan view of the experimental arrangement.

Fig. 14. Beam optics of the K3-L mode.

Fig. 15. Flux of the $\bar{p}$ beam as a function of the beam momentum, corresponding to 10^{12} extracted protons at 12 GeV/c on a Pt target 40 mm long and 6 X 10 mm^2 in cross section. The momentum bite accepted is ± 2 %.

Fig. 16. Exploded view around the liquid hydrogen target region.

Fig. 17. Schematic representation of the MWPC readout.

Fig. 18. $\ln(N_B/N_T)$ plotted versus the uncorrected beam momentum, where N_B is the number of incoming antiprotons and N_T the number of transmitted antiprotons which reached C6.

Fig. 19. $\bar{p}p$ total cross section plotted versus the corrected beam momentum. The data are preliminary and uncorrected.

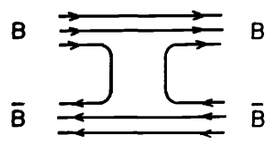

Fig. 1.

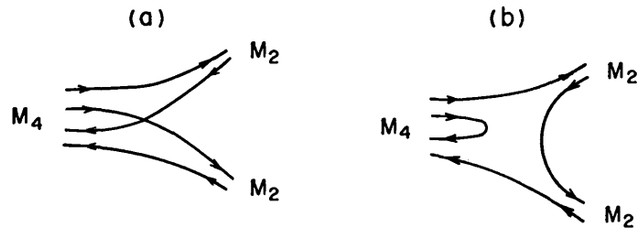

Fig. 2.

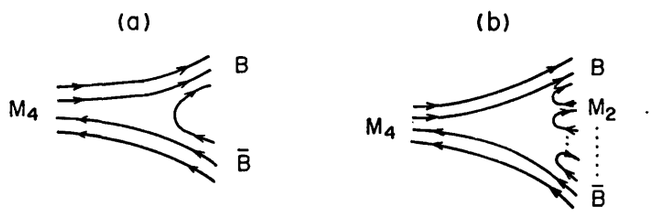

Fig. 3.

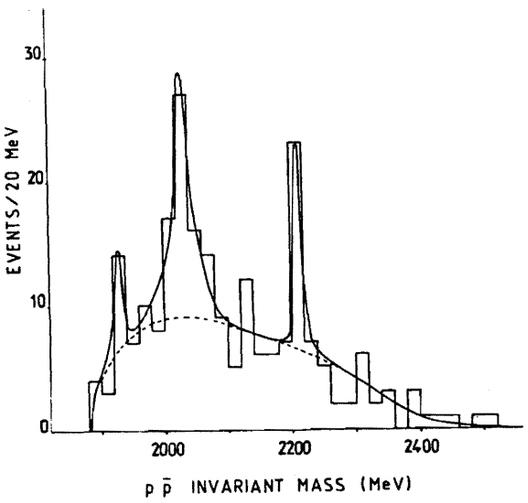

Fig. 4.

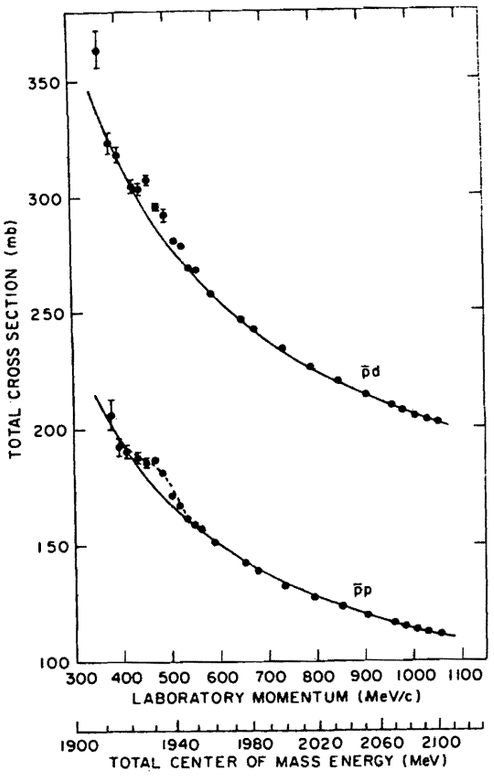

Fig. 5.

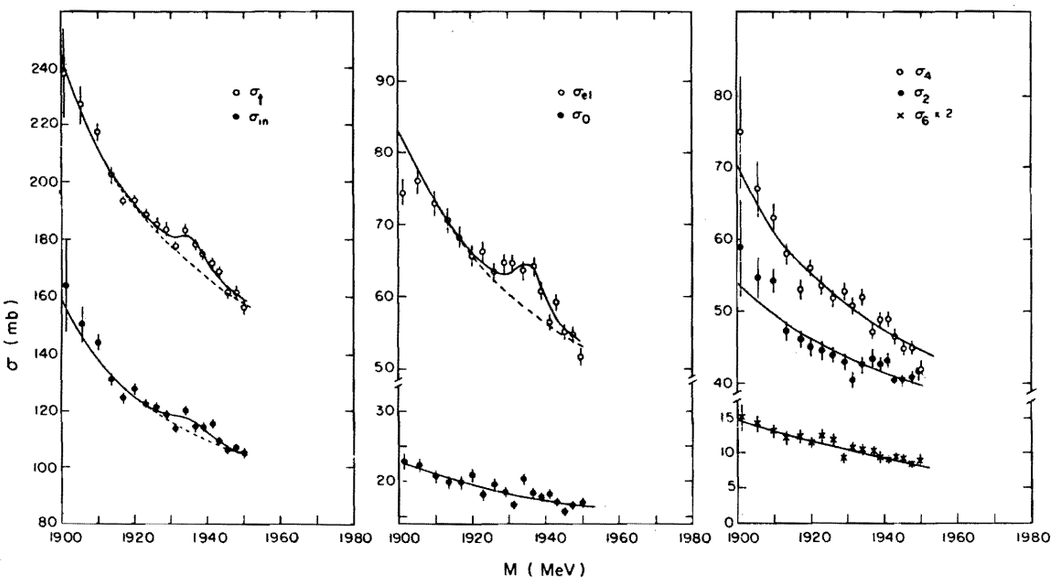

Fig. 6.

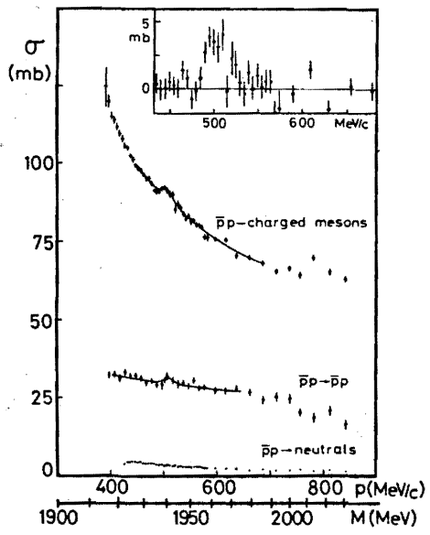
σ
(mb)
5
mb
0
500
600
MeV/c
100
75
50
25
0
p̄p–charged mesons
p̄p–p̄p
p̄p–neutrals
400
600
800
p(MeV/c)
1900
1950
2000
M(MeV)

Fig. 7.

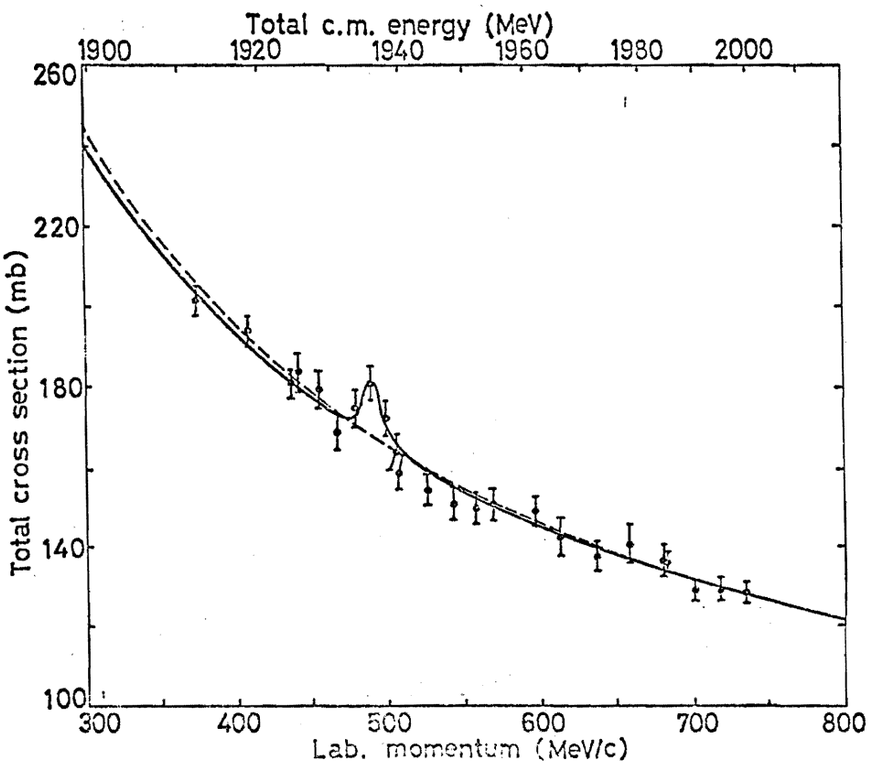
Total c.m. energy (MeV)
1900
1920
1940
1960
1980
2000
260
220
180
140
100
Total cross section (mb)
300
400
500
600
700
800
Lab. momentum (MeV/c)

Fig. 8.

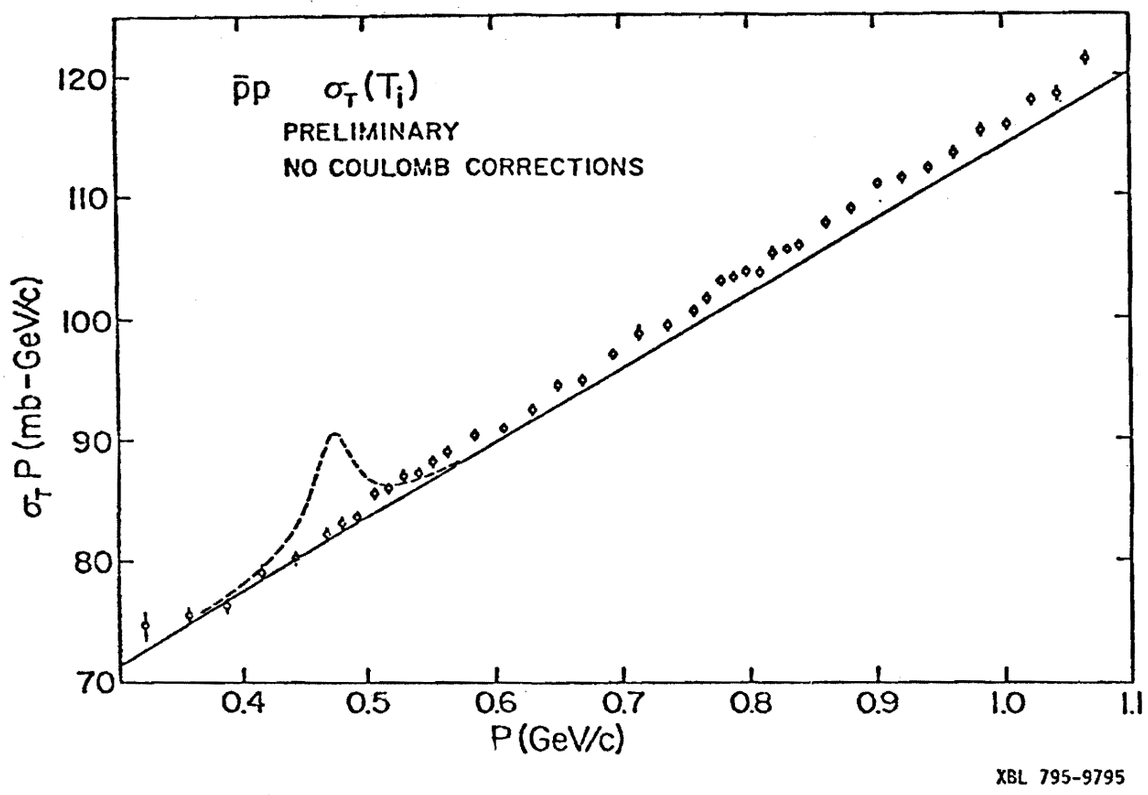
$\bar{p}p$ $\sigma_T(T_i)$
PRELIMINARY
NO COULOMB CORRECTIONS
$\sigma_T P$ (mb-GeV/c)
P (GeV/c)
120
110
100
90
80
70
0.4
0.5
0.6
0.7
0.8
0.9
1.0
1.1
XBL 795-9795

Fig. 9.

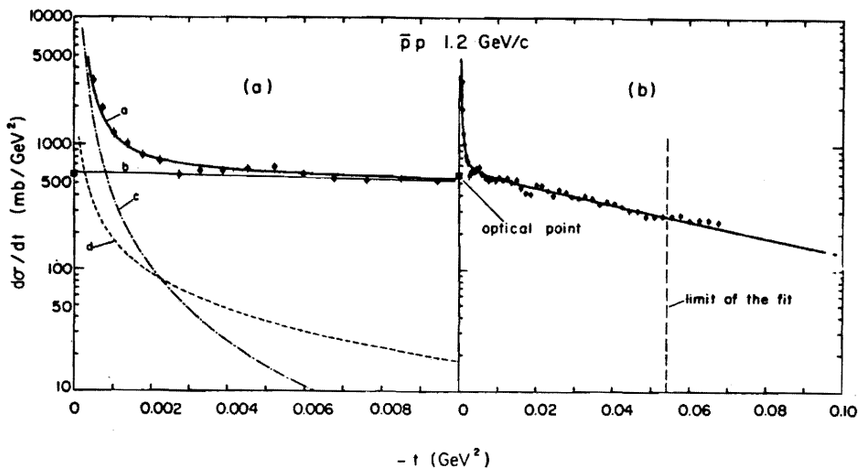
$\bar{p}p$ 1.2 GeV/c
(a)
(b)
a
b
c
d
optical point
limit of the fit
$d\sigma/dt$ (mb/GeV^2)
$-t$ (GeV^2)
10000
5000
1000
500
100
50
10
0
0.002
0.004
0.006
0.008
0
0.02
0.04
0.06
0.08
0.10

Fig. 10.

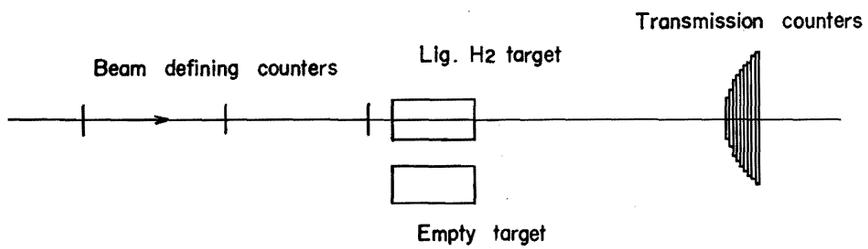

Fig. 11.

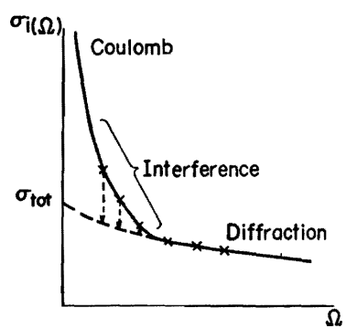

Fig. 12.

Experimental Set-up of $\bar{P}P$ Total Cross Section Measurement

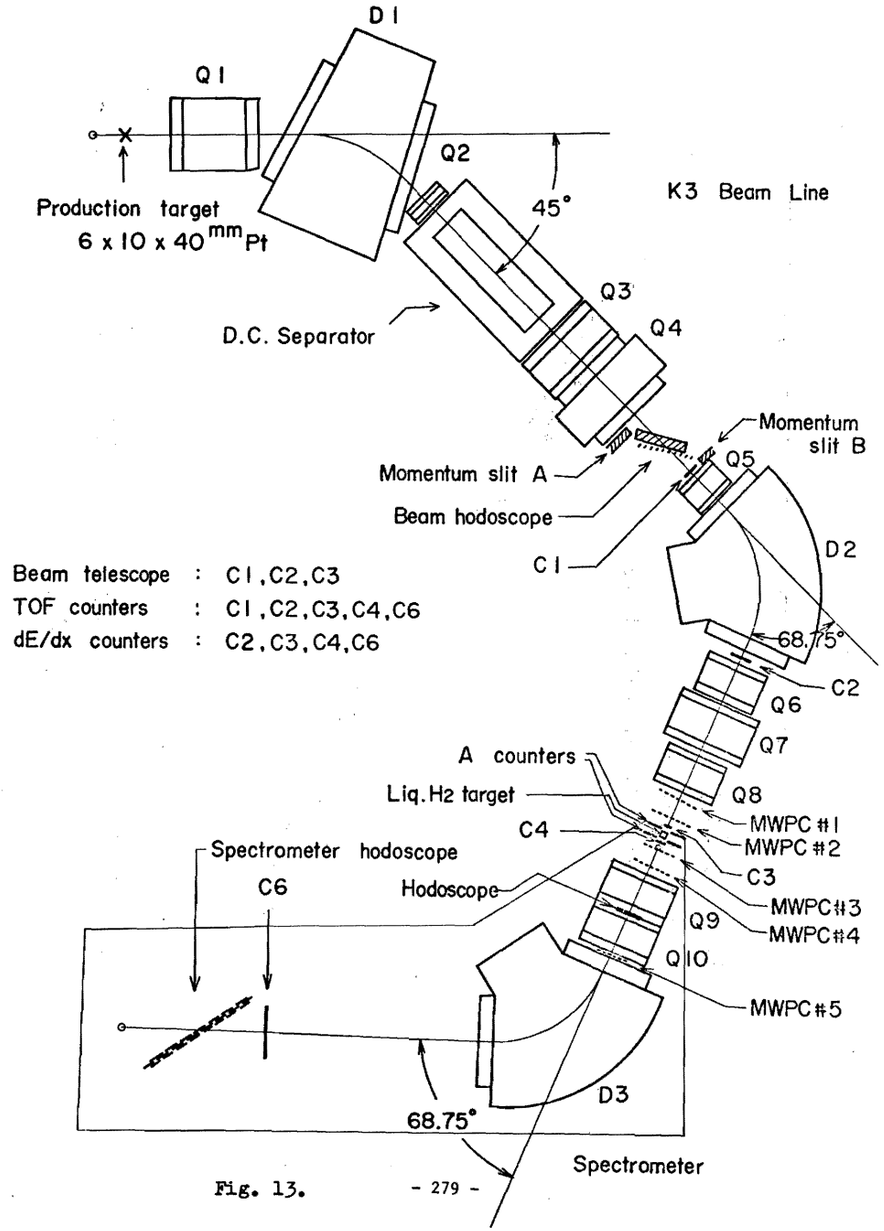

Fig. 13.

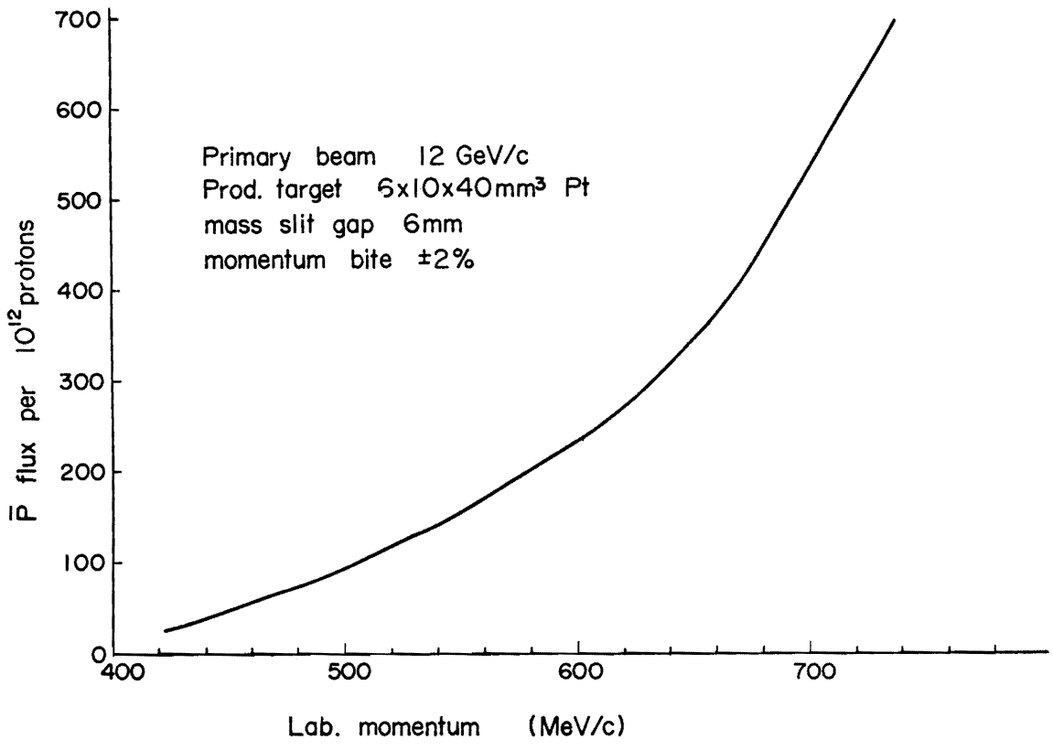
Primary beam 12 GeV/c
Prod. target 6x10x40mm³ Pt
mass slit gap 6mm
momentum bite ±2%
p̄ flux per 10¹² protons
Lab. momentum (MeV/c)

Fig. 15.

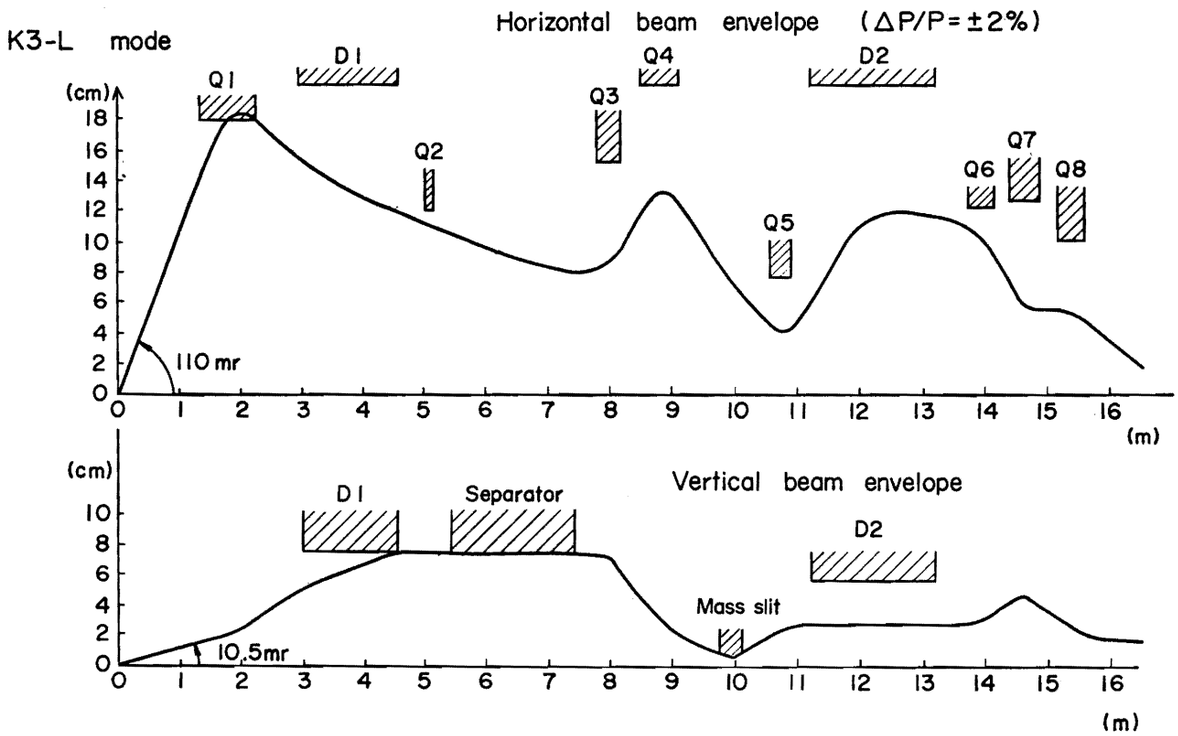
K3-L mode
Horizontal beam envelope (ΔP/P=±2%)
Q1
D1
Q2
Q3
Q4
D2
Q5
Q6
Q7
Q8
110 mr
(cm)
(m)
Vertical beam envelope
D1
Separator
D2
Mass slit
10,5mr

Fig. 14.

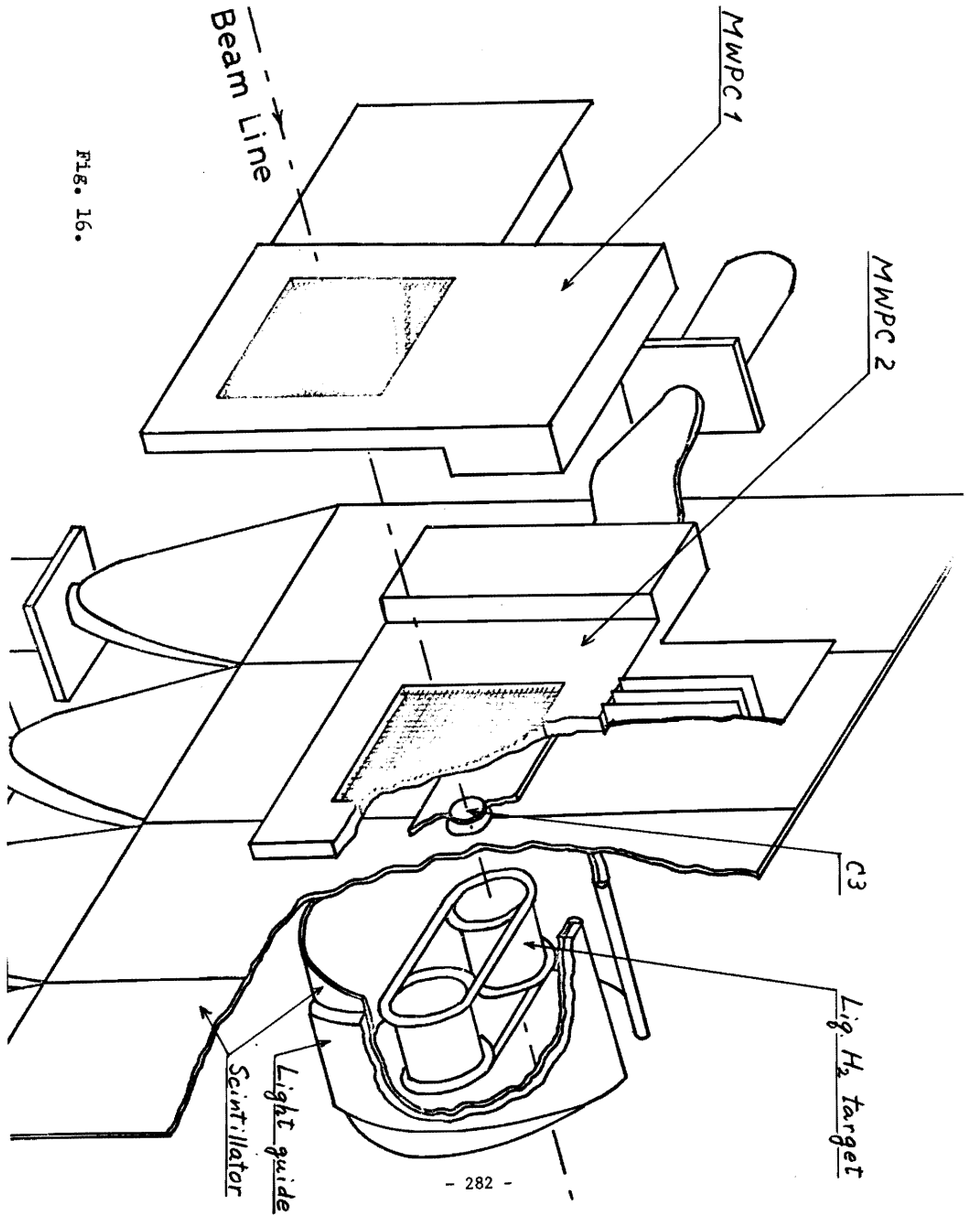
Beam Line
MWPC 1
MWPC 2
C3
Liq. H_2 target
Light guide
Scintillator

Fig. 16.

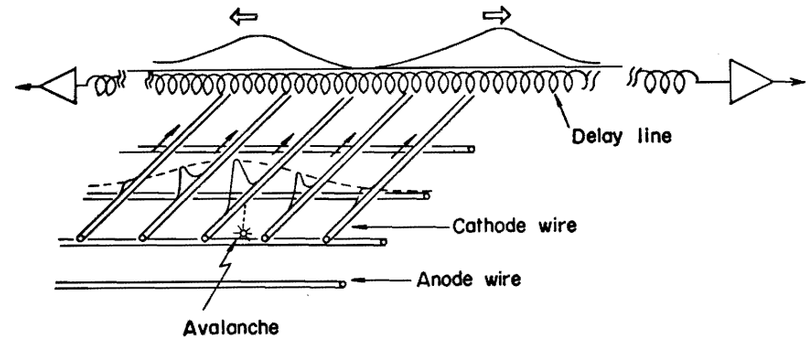
Delay line
Cathode wire
Anode wire
Avalanche

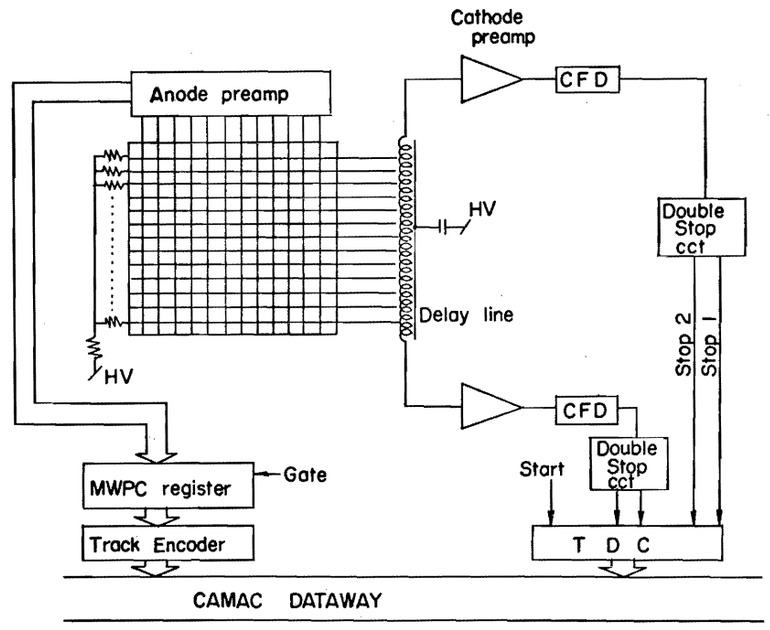
Cathode preamp
Anode preamp
CFD
HV
Double Stop cct
Delay line
Stop 2
Stop 1
HV
CFD
Double Stop cct
Start
MWPC register
Gate
Track Encoder
T D C
CAMAC DATAWAY

Fig. 17.

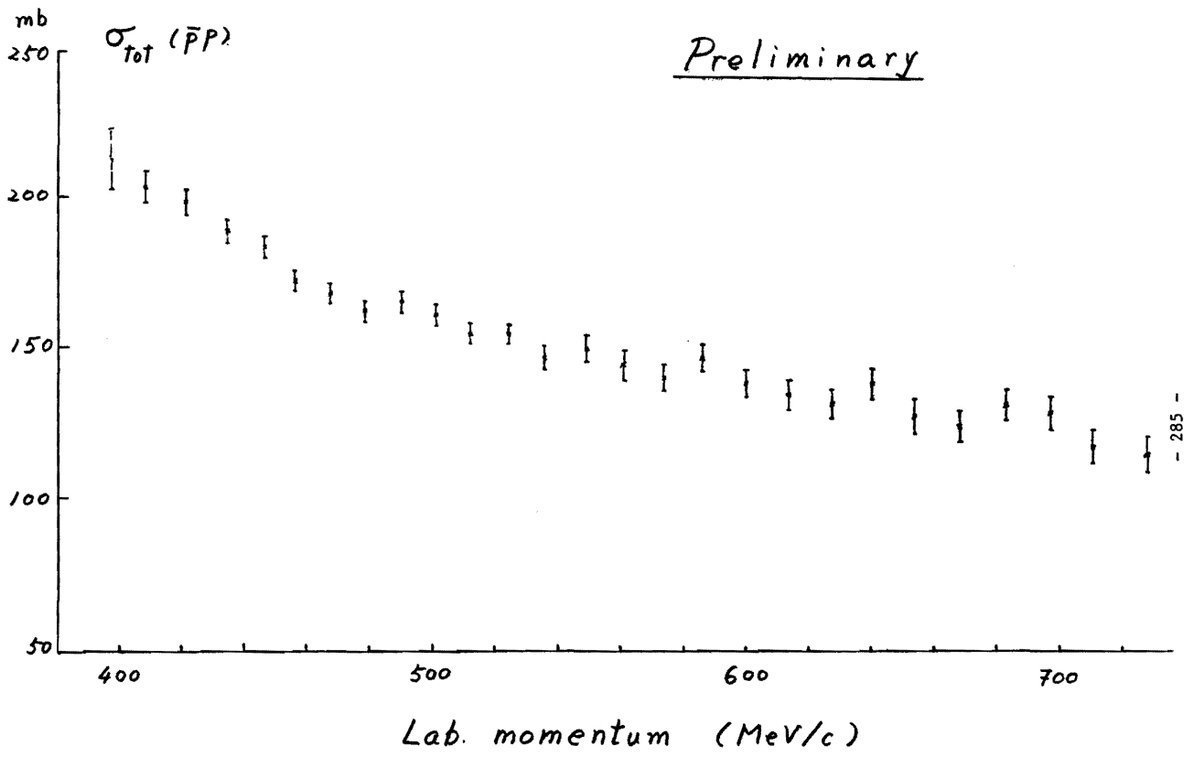
mb
σ_{tot} ($\bar{P}P$)
Preliminary
250
200
150
100
50
400
500
600
700
Lab. momentum (MeV/c)

Fig. 19.

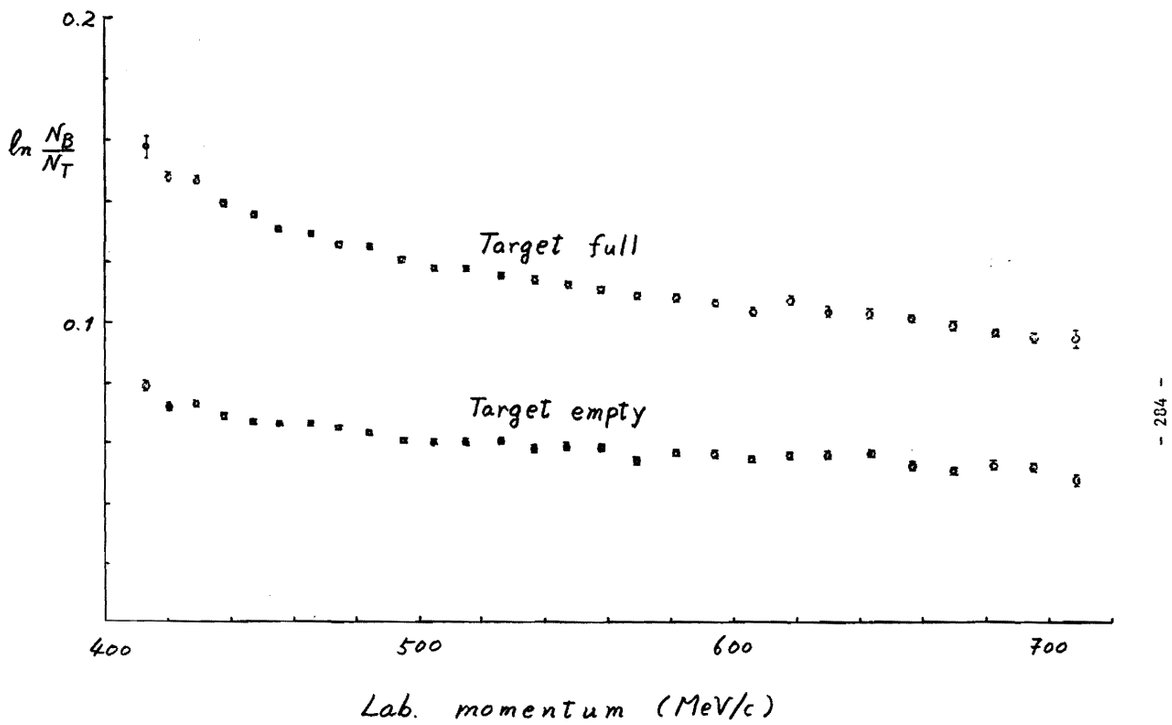
0.2
$\ln \frac{N_B}{N_T}$
0.1
Target full
Target empty
400
500
600
700
Lab. momentum (MeV/c)

Fig. 18.